Analysis of Plume Infrared Signatures of S-Shaped Nozzle Configurations of Aerial Vehicle

C. H. An[1], D. W. Kang[1], S. T. Baek[1], and R. S. Myong[2]
Gyeongsang National University, Jinju, Gyeongnam 52828, Republic of Korea

W. C. Kim[3]
Agency for Defense Development, Yuseong, Daejeon 34188, Republic of Korea

and

S. M. Choi[4]
Chonbuk National University, Jeonju, Chonbuk 54896, Republic of Korea

The IR susceptibility of the propulsion system of an aircraft is significantly affected by nozzle shapes and atmospheric conditions. To examine the effects of nozzle shapes and atmospheric conditions, various nozzle shapes were selected by considering a representative low-observable UAV and its propulsion system. Then, using the density-based Navier-Stokes-Fourier CFD code, the thermal flow field and the distribution of chemical species within a plume, which are essential for the analysis of IR signatures, were calculated. From the analysis of plume IR signatures for non-circular nozzles, it was found that IR signature levels were reduced significantly in the axial direction. However, relatively higher signature levels were observed on the left and right sides and below the nozzle due to increase in the aspect ratio of the nozzle outlet as well as curvature, which led to a wider distribution of the plumes along a downward slope. Further, in order to take into account atmospheric effects, the atmospheric transmissivity according to changes of season and observational distance was analyzed in detail. Finally, the lock-on range was calculated for different nozzle configurations and was compared with the basic circular shape.

[1] Graduate Student, Department of Mechanical and Aerospace Engineering, 501 Jinjudaero.
[2] Professor, Department of Mechanical and Aerospace Engineering and Research Center for Aircraft Parts Technology, 501 Jinjudaero; *myong@gnu.ac.kr*. Associate Fellow AIAA (Corresponding Author).
[3] Senior Research Engineer, P.O. Box 35.
[4] Professor, Department of Aerospace Engineering, 567 Baekjedaero.

Nomenclature

AR = aspect ratio

H_{inlet} = length of minor axis of nozzle inlet (m)

H_{outlet} = length of minor axis of nozzle outlet (m)

I_c = contrast intensity of infrared emission from aircraft (W/sr)

L = length of nozzle (m)

M-L = medium-large

NEI = noise equivalent irradiance

S-M = small-medium

S/N = signal-to-noise ratio

R_{LO} = lock-on range

w = wall condition

η_a = atmospheric transmission efficiency

κ_λ = optical thickness

λ = wavelength (μm)

ω = solid angle

$a_i(l)$ = incident-mean

$a_p(l)$ = Plank-mean

$a_\lambda(l)$ = spectral absorption coefficient

i'_λ = spectral intensity (W/m^2/μm/sr)

$i_{b,\lambda}$ = Plank blackbody intensity

$i_i(l)$ = average incident intensity with respect to wavelength

$i_b(l)$ = blackbody intensity

x = horizontal axis

y = vertical axis

I. Introduction

RECENT advancements in technologies for detecting infrared (IR) signatures [1,2] have made it easier to detect aircraft and rotorcraft flying at low altitudes. In particular, the development of portable IR seeker missiles equipped with modern IR detectors has emerged as a major factor with significant impact on the survivability of aircraft [3]. Therefore, to improve the survivability of aircraft, which play an essential role in today's military operations, the development of technologies to reduce the susceptibility-related IR signals of aircraft remains critical.

The IR signatures of an aircraft are generated by the engine/nozzle, exhaust gas, heating due to exhaust gas, aerodynamic surface heating, surface emission, anti-icing and de-icing systems, and reflection of the sun and the moon [4,5]. In particular, the IR signatures emitted from the exhaust gas generated from the propulsion unit of an aircraft and from the high temperature nozzle surfaces are easy targets for heat-seeking detectors. In the case of US military specification [6], the data of the maximum IR levels for the azimuth, elevation, bandpass (1-3, 3-5, 8-10, 10-12, 12-14 μm), altitude (sea level and 36,089 feet), and engine power settings (maximum, intermediate, and maximum continuous) are required. In this respect, technologies for reducing IR signature levels from the propulsion unit are regarded as essential for enhancing the survivability of an aircraft. In particular, it is critical to ensure that the propulsion unit of an aircraft is designed to emit low-level IR signals during the initial stage of aircraft development, since it is difficult to modify the design once the development enters a late stage.

Studies for reducing aircraft plume IR signatures have been conducted by many researchers around the world. Thompson and Birk [7] released a test report that examined how an IR suppressor affected the infrared signatures generated by exhaust gas. Decher [8] analyzed the link between the shape of a nozzle outlet and IR signals. Recently, a research team led by Mahulikar [9-16] conducted research quantifying aircraft infrared signatures for numerical calculation, and also examined the effects of atmospheric transmission and radiance on aircraft infrared signatures. Based on this, the Mahulikar research team acquired data related to a method for numerically calculating aircraft infrared signatures and the effects of atmospheric conditions on IR signatures.

However, previous studies have mostly been based on the conventional circular nozzle shape and associated simplified plume model. Detailed analyses of IR signatures based on the thermal flow field information obtained with more accurate CFD method for various S-shaped nozzle configurations and atmospheric conditions have not been sufficiently conducted yet.

This study analyzed the effects of S-shaped nozzle configurations of a UAV and atmospheric conditions on plume IR signatures in order to reduce IR signature levels. First, the thermal flow fields at the nozzle and plume were computed by varying the aspect ratio and curvature of the nozzle outlet. Based on this data, aircraft IR signatures were analyzed to examine the link between nozzle shape changes and IR signatures. To that end, an analysis of engine performance was conducted using a program called AEDsys [17] by referring to the missions and performance requirements of a representative low-observable UAV, and consequently a circular convergent nozzle meeting the mission requirements was designed. Various nozzle shapes were then designed by varying the aspect ratio and curvature of the nozzle outlet of an aircraft, starting with a basic circular nozzle. Analysis of the thermal flow fields was conducted using a compressible Navier-Stokes-Fourier code CFD-FASTRAN [18]. Based on the results of the analysis of thermal flow fields, the temperatures and components of nozzle plumes were also analyzed, and the IR signatures of aircraft plumes were calculated. Further, using LOWTRAN 7 [19], a program for analyzing atmospheric transmission, the effects of the change of season and observation distance on plume IR signatures were examined in detail. Finally, the lock-on range, the last element of the survivability analysis, was calculated for different nozzle configurations and was compared with the basic circular shape.

II. Selection of Nozzle Configurations of a UAV

A. Aircraft Performance Analysis and Design of the Basic Circular Nozzle

To analyze the characteristics of thermal flow fields at the rear fuselage of an aircraft, the initial conditions at the nozzle inlet and the design of the nozzle shape should be computed on the basis of a performance analysis of the aircraft engine. The most important factor in an engine performance analysis is determining the requirements of the engine. The requirements of an engine tend to vary depending on the mission of the aircraft. In this study, the AEDsys program was utilized for analyzing the engine performance of a representative subsonic UAV.

The thrust of the aircraft engine can be calculated through a mission analysis by referring to the missions and performance of the UAV. The pressure, temperature, efficiency, and mass flow were then calculated by determining the design values for the major engine components. In this study, we consider a convergent nozzle designed to meet the requirements for cruising at an altitude of 11 km at the subsonic speed of Mach 0.8. As shown in Fig. 1, the mission of the UAV was assumed to include take-off, acceleration and climb, cruising at subsonic speed, loitering, striking a target, cruising at top speed, and landing. Table 1 shows the geometry and inlet conditions of a circular convergent nozzle that was designed by the analysis of the mission and performance.

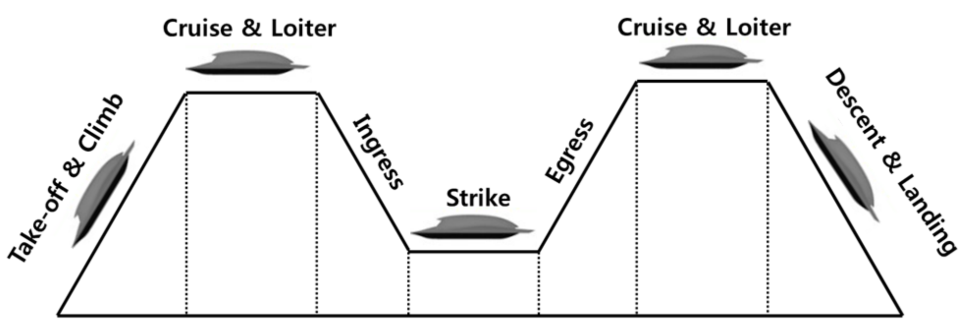

Fig. 1 Mission profile of a UAV.

B. Design of S-Shaped Nozzle Configurations

To examine the effects of nozzle configurations on IR signature reduction, 20 nozzle shapes were considered by varying two design variables (the curvature and the aspect ratio) from the reference circular convergent nozzle. Since the characteristics of a nozzle depend on the cross-sectional area of the nozzle, the circular convergent nozzle identified through the analysis of engine performance was divided into nine equal parts from the inlet to the outlet. The areas of the nine parts determined in this manner were then identically applied to various nozzle shapes, leading to nozzles with exactly the same cross-sectional area distributions.

Table 1 Nozzle geometry and inlet conditions.

Nozzle geometry	Inlet (m^2)	0.18232
	Outlet (m^2)	0.12617
	Length (m)	0.964
Inlet condition	Mass flow (kg/sec)	17.19
	Specific heat ratio	1.3477
	Static pressure (Pa)	104,740
	Static temperature (K)	629.86
	Mach number	0.4454

The nozzle inlet was created in a circular shape, while the outlet was made to have an oval shape with a surface area identical to that of the circular nozzle. The oval shape was designed by applying an aspect ratio suitable for each case. The cross-sectional area of the middle part of a non-circular nozzle with a specified outlet aspect ratio can be calculated using a hyperbolic tangent function, which can provide a mathematically simple form to generate various shapes found in UAV engine nozzles,

$$y = (H_{inlet} - H_{outlet}) \times \tanh(4x / L)\,, \tag{1}$$

where the x-coordinate represents the axial distance from the inlet to the outlet. Based on this formula, a non-circular nozzle with different outlet aspect ratios can be designed by producing an ellipse having the y-coordinate as its minor axis and the z-coordinate as its major axis. Also, a total of four different curvatures were considered by applying the hyperbolic tangent function to the four points: the upper-most line of the minor axis, and the points 1/4, 1/2, and 3/4 from the upper-most line of the minor axis. Figure 2 shows the various nozzle configurations designed in this manner.

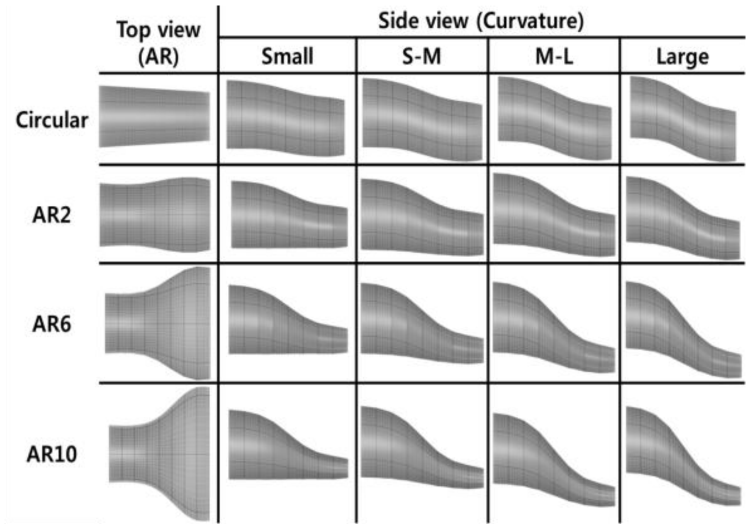

Fig. 2 Various nozzle shapes.

III. CFD Analysis of Thermal Flow Field

A. Computational Grid and Boundary Condition

The nozzle flows generated by high-pressure and high-temperature gases consist of various complicated flow features and their interaction like shock and expansion waves, wall boundary layers, and shear layers. To cover these flows effectively, the size of the external flow field of the computational domain was set to be 30, 50 times of the diameter of the nozzle inlet in the radial and axial direction, respectively. Figure 3 shows the computational grid, boundary conditions, and the composition ratio of the chemical species used for the calculation.

The flow and thermal conditions determined through the engine performance analysis using AEDsys were applied to the nozzle inlet. The no-slip flow and the adiabatic thermal conditions were then applied to the nozzle wall where an insulating material is usually used. Lastly, the pressure boundary condition maintained with the outside atmospheric pressure at the corresponding altitude was applied to the outlet. A structured mesh with approximately one million cells was used.

For a detailed analysis of plume IR signatures, it is important to describe accurately the components of chemical species in both the internal exhausted gas and the external air, since chemical species in the atmosphere may have different effects on plume IR signatures. In this study, the chemical species representing the composition of the atmosphere—78% of nitrogen N_2, 21% of oxygen O_2, and 1% of carbon dioxide CO_2—were considered for the external air of the nozzle. In the case of the internal nozzle flow, the gaseous chemical species were assumed to consist of 74% of nitrogen N_2, 13% of water vapor H_2O, and 13% of carbon dioxide CO_2, which are produced through the complete combustion of a jet fuel with a molecular structure of $C_{11}H_{22}$.

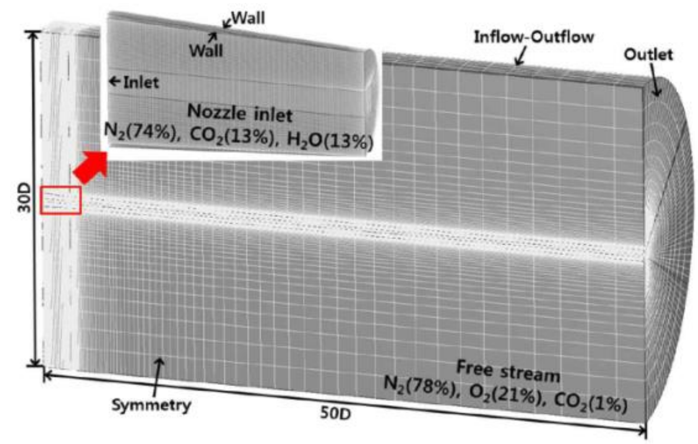

Fig. 3 Numerical boundary conditions.

B. Validation of Thermal Flow Field Analysis

To conduct the thermal flow field analysis for the plume and the inside of the nozzle, a compressible Navier-Stokes-Fourier code CFD-FASTRAN was used [20]. This enabled the analysis of high subsonic, supersonic, and transonic flow domains, which entail shock waves and jet boundaries. In the code, the density-based and cell-based finite volume method, implicit time stepping method were used. The $k-\varepsilon$ turbulence model [21], which is known suitable for jet flows, was used. In addition, the thermal flow field was assumed to be not far from thermal equilibrium, and the Fick principle was used for the mass diffusion of the chemical species.

By following the verification and validation practice described by Oberkamp and Roy [22], a validation study was conducted to check the accuracy of the present computational method. The thermal flow field of a convergent nozzle, as presented in a paper by Thornock et al. [23], was first considered. For validation, the location of sonic lines for the case of a nozzle pressure ratio (NPR) defined (between the nozzle inlet and external atmosphere) as 2.5, and three nozzle convergence angles of 15°, 25°, and 40°, were examined. In Fig. 4, it was found that the sonic lines gradually move rearward as the nozzle convergence angle increases, and the (approximate) theoretical values are qualitatively consistent with the CFD results. On the other hand, the CFD results were shown to be in better agreement with the experimental results than the (approximate) theoretical predictions; in particular, for the location of sonic lines at higher nozzle angles.

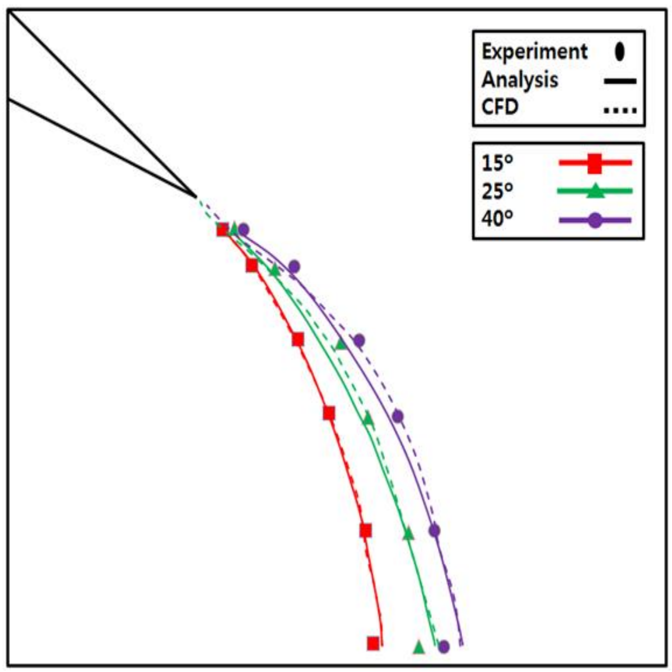

Fig. 4 Sonic lines for various nozzle angles in the case of NPR 2.5.

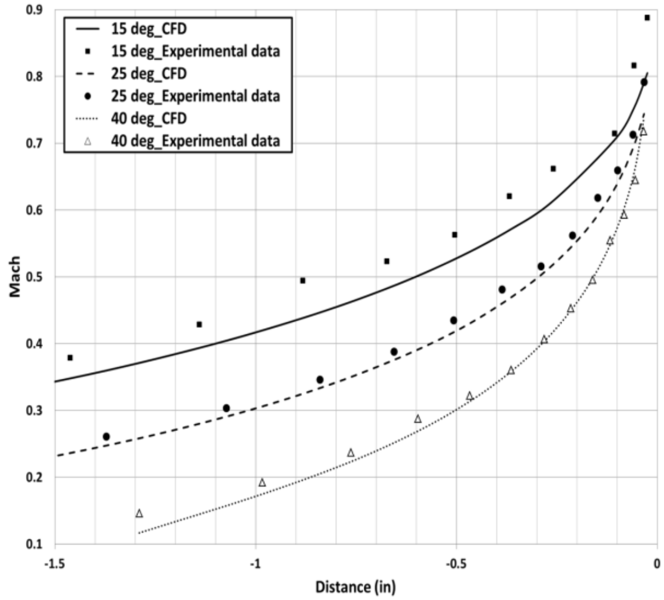

Fig. 5 Comparison of CFD result and experimental data in the case of NPR 2.0.

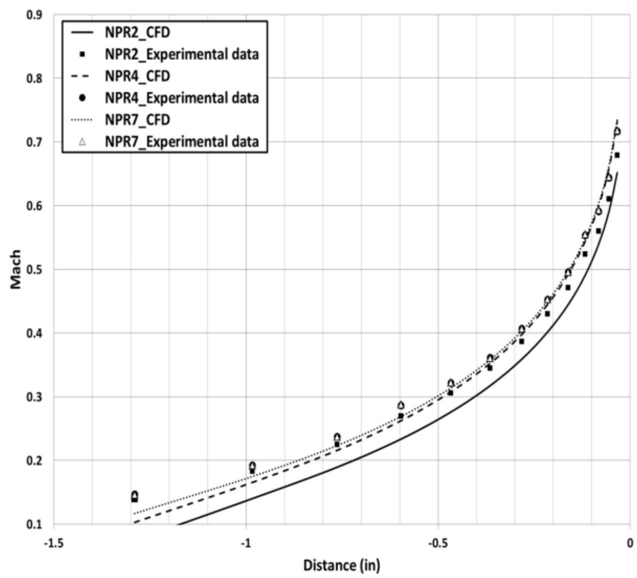

Fig. 6 Comparison of CFD result and experimental data in the case of convergence angle 40°.

For additional validation of the present CFD method based on a commercial code CFD-FASTRAN, experimental data regarding the Mach number distribution near the wall of a nozzle operating on the ground, which were reported in the AIAA Propulsion Aerodynamics Workshop [24], were considered.

The Mach number distributions near the nozzle wall were compared for the NPR 2.0 case with three convergence angles of 15°, 25°, 40°, and for the angle 40° case with an NPR of 2.0, 4.0, and 7.0. From Figs. 5 and 6, it can be seen that the CFD results are in close agreement with the experiment data of the Mach number. Also, it was found that the accuracy of the computational analysis improves as the values of the convergence angle and the NPR increase. Based on this validation study, the NPR value of 4.6 was determined to be high enough for the present S-shaped nozzle configurations of a UAV, and it was expected that accurate computational results of thermal flow fields, in particular, the Mach number, a quantity closely related to the temperature, would be achieved.

IV. IR Signature Analysis

A. Calculation of Spectral Intensity Based on the Narrow Band Model

When analyzing the susceptibility characteristics associated with aircraft IR signatures, the characteristics of IR signals generated from the rear fuselage and plumes are considered important factors. In this study, the narrow band model considered by Grosshandler [25] and Mahulikar *et al*. [11] was applied to calculate plume IR signatures. This model enables the calculation of the average radiation properties in a section of IR wavelength, and is considered more efficient compared to the line-by-line band model, which requires longer calculation time.

In this model, the key concept is based on a statistical chart for the molecular model and absorption coefficients with respect to the elements in a straight line based on the radiative heat transfer equation, where absorption and release of radiative heat occur without scattering. Based on the results of a thermal flow field analysis, such as the temperature, partial pressure of the atmospheric components at a particular point of the plume area, the spectral intensity can be calculated through the following equation

$$\begin{gathered} i'_\lambda(l) = i'_{\lambda,w} e^{-\kappa_\lambda(l)} + \int_0^{\kappa_\lambda(l)} i_{b,\lambda}(l^*) \exp[-\kappa_\lambda(l) + \kappa_\lambda(l^*)] d\kappa_\lambda(l^*), \\ \kappa_\lambda \equiv \int_0^l a_\lambda(l^*) dl^*. \end{gathered} \tag{2}$$

The average spectral intensity incident on a differential volume from all directions can then be calculated by integrating the spectral intensity over solid angle ω:

$$\overline{i_\lambda(l)} = \frac{1}{4\pi}\int i'_\lambda(l)d\omega. \tag{3}$$

Also, two different spectrally averaged absorption coefficients (the incident-mean and the Planck mean) can be defined:

$$a_i(l) \equiv \frac{1}{i_i(l)}\int_0^\infty \overline{i_\lambda(l)}a_\lambda(l)d\lambda,\ a_p(l) \equiv \frac{1}{i_b(l)}\int_0^\infty i_{b,\lambda}(l)a_\lambda(l)d\lambda, \tag{4}$$

whose denominators are the average incident intensity (integral of the average spectral intensity over wavelength) and the blackbody intensity, respectively. The radiative heat transfer was calculated using the data between two points in the computational domain. That is, the calculation of spectral intensity during the plume IR signature analysis was conducted by using the temperature, pressure, and partial pressure values at each point defined by dividing a straight line connecting any two points.

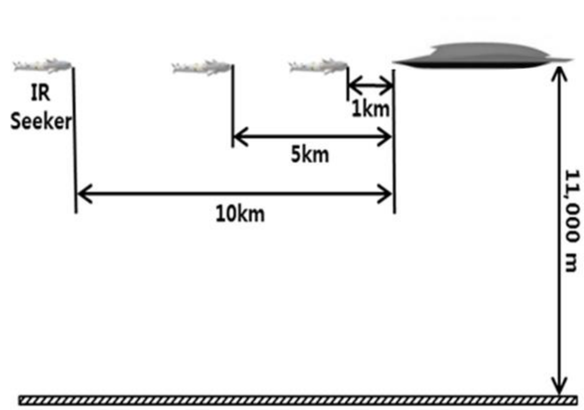

Fig. 7 The seeker positions used in calculation of atmospheric transmissivity.

B. Calculation of Atmospheric Transmission Using LOWTRAN 7

To predict aircraft IR signatures detected by an infrared detector, the transmission level of IR signatures initially generated from an aircraft to the infrared detector should be calculated. To this end, the LOWTRAN 7 model was used to calculate atmospheric transmissions for different seasons and observational distances at a particular altitude. More specifically, the calculation was made based on the seasonal conditions of summer and winter, and the representative atmospheric model, and observational distances of 1 km, 5 km, and 10 km. The altitude of the observed object was set to be 11 km, which is close to the actual flying altitude of an aircraft, and the position of the observer was assumed to be directly behind the nozzle, as illustrated in Fig. 7. The calculated value of atmospheric transmission was then applied to the analysis of plume IR signatures based on the narrow band model.

V. Results

A. Results of Thermal Flow Field According to Nozzle Shape Variations

The computational results of the nozzle flow of an aircraft cruising at an altitude of 11 km and speed of Mach 0.8 showed that, compared to the circular nozzle, the average temperature at the outlet of various nozzle shapes decreases as much as 6.1% (30K), and the highest temperature near the nozzle wall drops up to 6.0% (33K). Also, in order to take into account the effects of penalties caused by the nozzle shape variations, the thrust of the nozzle was calculated based on the pressure, velocity, and mass flow at the nozzle outlet of computational domains. The thrust level of various nozzle shapes was found to decrease as much as 10.7% compared to the circular nozzle, and the degree of thrust reduction became larger as the aspect ratio or curvature increased. This is because the pressure at the nozzle outlet is changed due to nozzle shape variations. Table 2 shows the average and highest temperatures at the nozzle outlet and wall for various nozzle configurations.

Table 2 Comparison of exit/wall temperature and thrust for various nozzle configurations.

Exit AR	Curvature	Exit temperature (K)		Wall temperature (K)		Thrust (N)	Exit AR	Exit temperature (K)		Wall temperature (K)		Thrust (N)
		Average	Max	Average	Max			Average	Max	Average	Max	
Circular	-	487.1	493.5	553.4	564.0	5152.3	6.0	479.0	485.6	537.9	560.9	5020.3
	Small	485.2	492.7	548.3	566.0	5135.4		481.0	485.7	537.2	569.7	4980.7
	S-M	485.0	492.6	549.1	568.6	5129.7		480.1	495.6	535.8	573.8	4940.1
	M-L	484.6	492.5	548.2	571.2	5120.9		479.2	501.7	532.9	578.0	4870.3
	Large	483.9	493.0	547.1	573.6	5107.3		467.4	508.1	520.1	583.6	4697.7
2.0	-	483.1	490.6	540.4	561.7	5042.2	10.0	477.0	487.7	535.9	562.5	5010.5
	Small	485.6	491.9	540.2	564.0	5029.8		478.5	508.4	534.8	572.3	4908.6
	S-M	485.3	492.4	539.7	566.5	5017.8		477.6	509.8	532.7	576.8	4900.8
	M-L	484.9	493.9	538.8	569.2	4999.7		471.5	515.8	526.2	582.0	4782.7
	Large	484.3	496.1	537.5	570.2	4849.2		457.3	525.6	522.5	588.2	4602.2

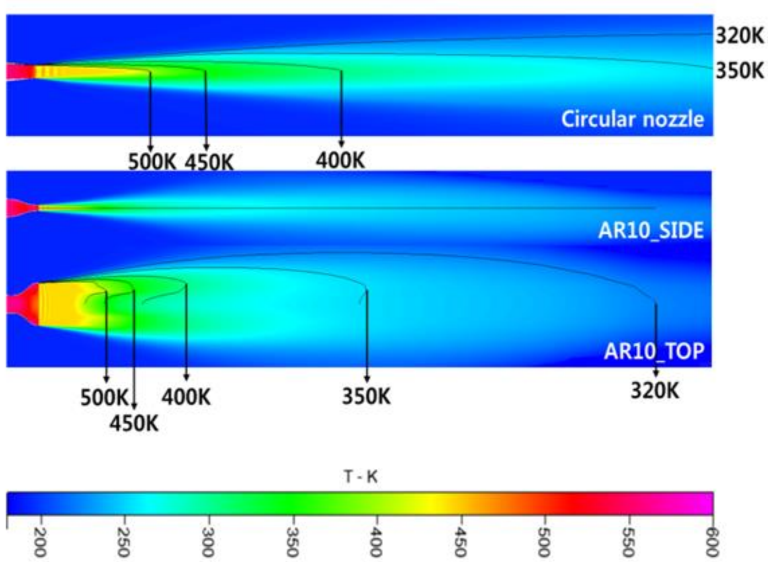

Fig. 8 Plume temperature distribution for circular and AR10 nozzles.

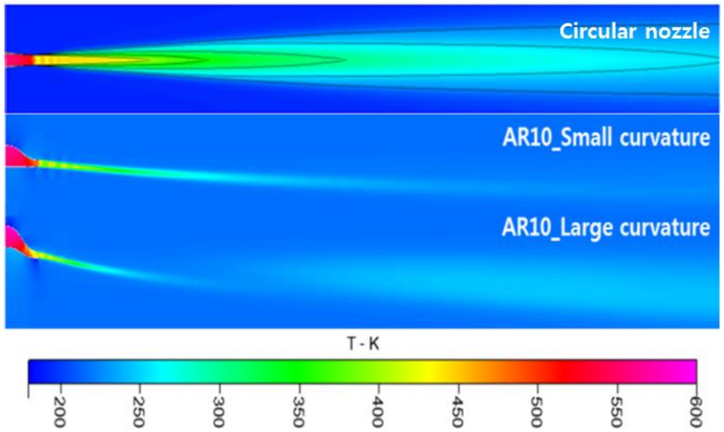

Fig. 9 Plume temperature distribution for various nozzle shapes.

As shown in Fig. 8 of the temperature distributions of aircraft plumes for a high aspect ratio case (10.0), the length of nozzle plumes was considerably shortened and the core plume was widened from side to side in comparison with the circular nozzle. For example, in the case of 350 K temperature contours, the plume length of the nozzle with the aspect ratio 10.0 was reduced to as much as half of that of the basic circular nozzle. This is because high-temperature gases exhausted from the nozzle (with the inlet condition of 630 K and M=0.45) were distributed widely to the left and right as the aspect ratio at the nozzle outlet increased, and were then mixed with the cold air of the external atmosphere (217 K, M=0.8). Also, as shown in Fig. 9, the substantial shortening of core plumes remained the same for enhanced curvature cases. In addition, the plumes tended to form downward compared to the circular nozzle when the large curvature was applied. This is because the nozzle outlet is located considerably lower than the nozzle inlet when a large curvature is applied, leading to a slope between the nozzle inlet and outlet. Along this slope, the flow from the nozzle outlet is formed downward, which will consequently change the plume IR signatures and the nozzle thrust. Therefore, it can be summarized that, although both of aspect ratio and curvature contributed to the reduction of the temperature in the plumes, the aspect ratio played more dominant role in the shortening of core plumes.

B. Results of Plume IR Signature

Figure 10 shows the effects of nozzle shape variations—the aspect ratio and curvature—on plume IR signatures. In this calculation, the location of an observer was assumed to be directly behind the nozzle (20m distance). The plume IR signatures were found to be reduced up to 76% in the 4-4.5μm band in comparison with the circular nozzle. Also, in all wavelengths including 4-4.5μm for CO_2 and 6-7μm for H_2O, IR signatures were reduced in proportion to the nozzle curvature and aspect ratio. This is in line with the results of the thermal flow field analysis, and is directly related to the outcome that the plumes produced by nozzles with higher aspect ratio and larger curvature have lower temperatures on average. Also, compared to those of the circular nozzle, these plumes have shorter lengths and tend to be more widely distributed.

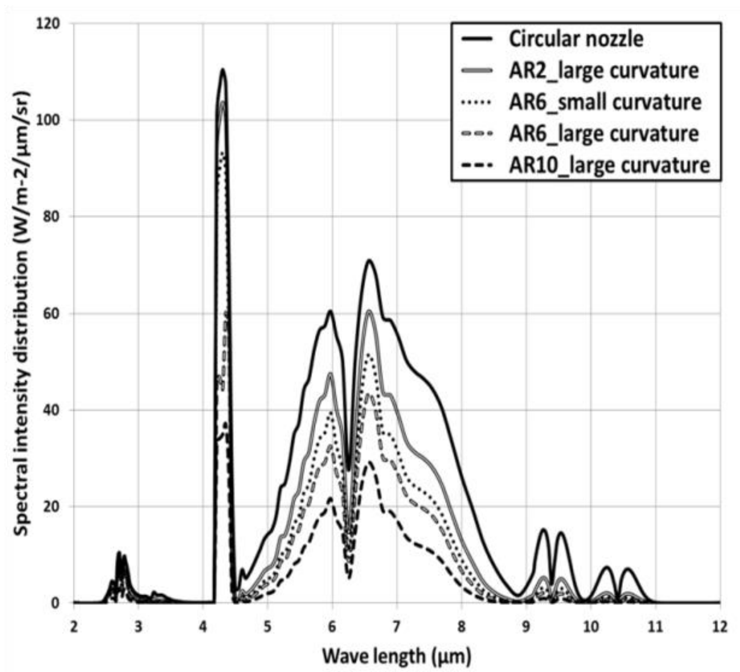

Fig. 10 Plume IR signature for various nozzle shapes.

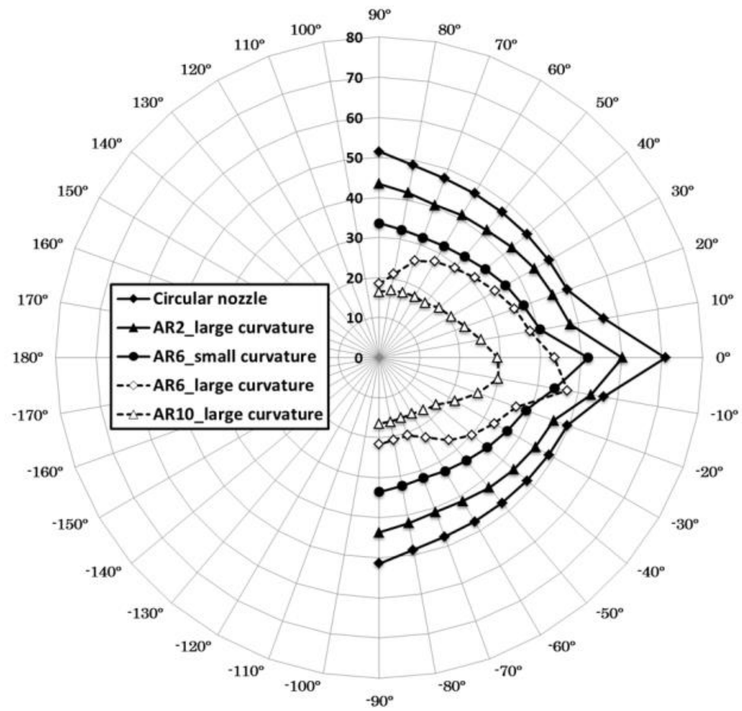

Fig. 11 Maximum IR signature ($W/m^2/\mu m/sr$) in the 5-8μm band for different elevation angles.

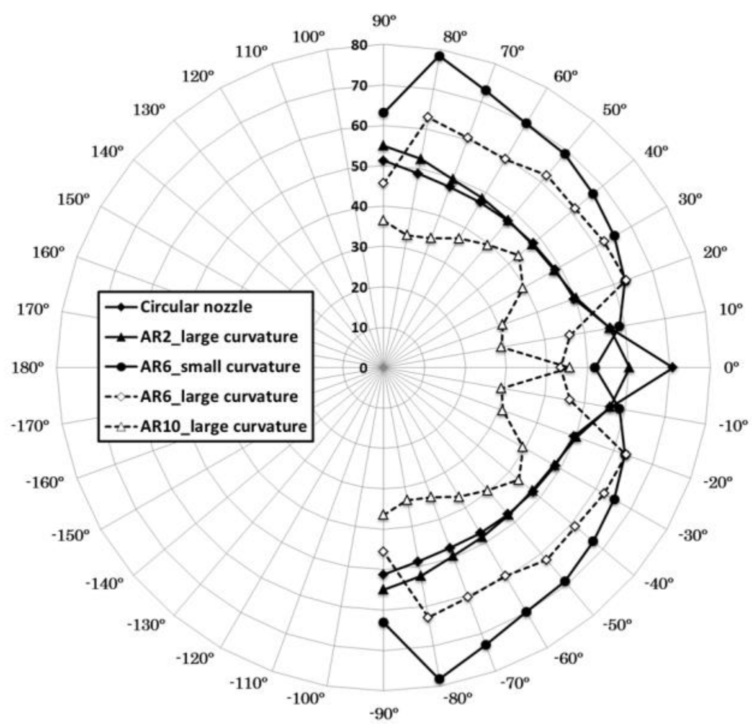

Fig. 12 Maximum IR signature ($W/m^2/\mu m/sr$) in the 5-8μm band for different azimuth angles.

To examine the effects of the aspect ratio and curvature of the nozzle with respect to the observation location, as a sample case, the IR signature in the 5-8μm band was calculated by changing the elevation and azimuth angles by 10°, which is similar to the practice specified in MIL-E-5007D [6]. As shown in Figs. 11 and 12, the IR signatures were reduced, primarily due to the enhanced mixing with cold free-stream air, in proportion to the nozzle curvature and aspect ratio in most cases. Further, the maximum IR signatures were found to be higher in the direct rear and at around 10° to the downward direction. This is because the plumes formed downward with the nozzle with large curvatures, and therefore high-temperature parts inside the plumes were captured more. In particular, in the case of a nozzle with an aspect ratio of 6.0 and a large curvature, the maximum IR signatures were found at around 10° to the downward direction, not in the direct rear.

When IR signatures were calculated at different azimuth angles, as shown in Fig. 12, IR signatures were observed to be higher on the left and right sides rather than on the direct rear in most cases. This is because the plumes were distributed widely to the left and right as the aspect ratio increased, and therefore high-temperature parts inside the plumes are captured more on the left and right sides of the nozzle.

In particular, IR signatures for the nozzle with an outlet aspect ratio of 6.0 and a small curvature were more noticeable compared to other oval-shaped nozzles, regardless of the location of an observer. The reason is that the plumes of this particular nozzle have a higher average temperature and are formed along a smaller downward slope, and consequently high-temperature parts of plumes are caught more at the wide range of azimuth angles. On the other hand, the IR signatures of the nozzle with an outlet aspect ratio of 2.0 were enhanced at the center, rather than on the right or left side, despite the non-circular shape of the nozzle outlet. A plausible explanation is that the plumes were not formed widely enough from side to side in that case.

C. Results with Consideration of Atmospheric Effects

The atmospheric transmissivity was calculated using LOWTRAN 7 for different seasons and observational distances. From Figs. 13 and 14, it can be noted that the atmospheric transmissivity in the 5.5-7.5μm band is lower in summer than in winter. This phenomenon is due to the fact that the higher concentration of H_2O in summer absorbs the signature more than in winter in the 5.5-7.5μm band. Also, as the observational distance becomes longer, the atmospheric transmissivity is lower, since the IR signatures initially emitted from an aircraft need to pass through more atmospheric components, and therefore more absorption of signatures takes place.

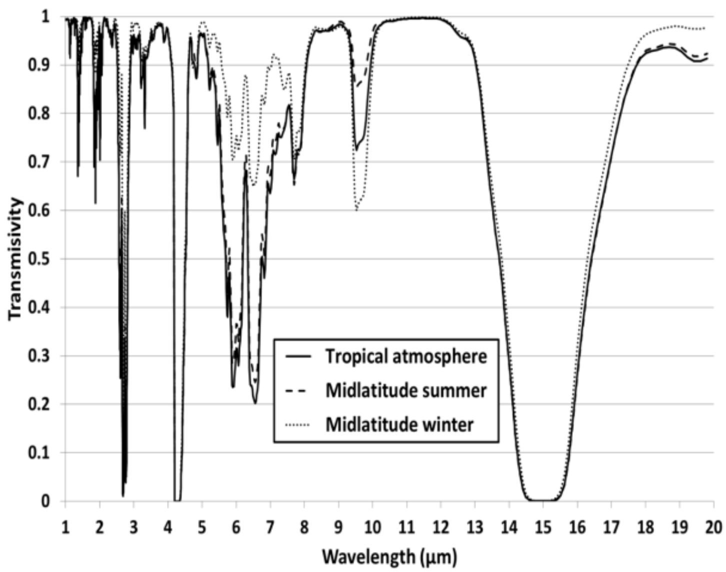

Fig. 13 Transmissivity for different seasons in the case of the observation distance 10 km.

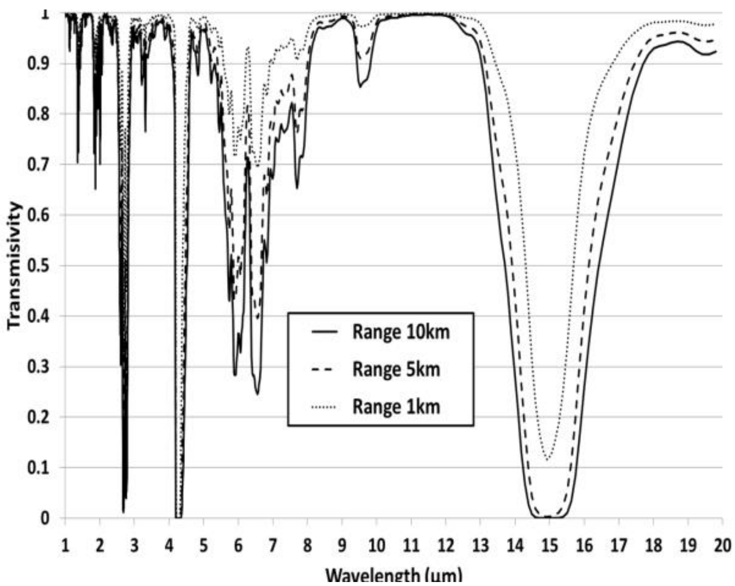

Fig. 14 Transmissivity for different distances in the case of the tropical atmosphere.

Moreover, to examine the effect of the location of the detector, a sample case where the detector was located at a lower altitude was considered. In Fig. 15, it can be seen that the atmospheric transmissivity is lower when the detector is located 10 km below the nozzle, in comparison with the case of a detector positioned at the same altitude. This is because IR signatures from the nozzle pass through a high density of CO_2 and H_2O in the atmosphere with on their way to the detector, during which more IR signatures are absorbed.

Meanwhile, in all cases, lower atmospheric transmissivity was observed in the wavelengths of 1.4μm, 1.9μm, 2.7-3.2μm, 4.3-4.5μm, 5.5-7.5μm, and 14-16μm. The polyatomic gaseous components in the atmosphere are responsible for this phenomena; H_2O in the wavelengths of 1.4μm, 1.9μm, and 5.5-7.5μm, and CO_2 in the wavelengths of 2.7-3.2μm, 4.3-4.5μm, and 14-16μm.

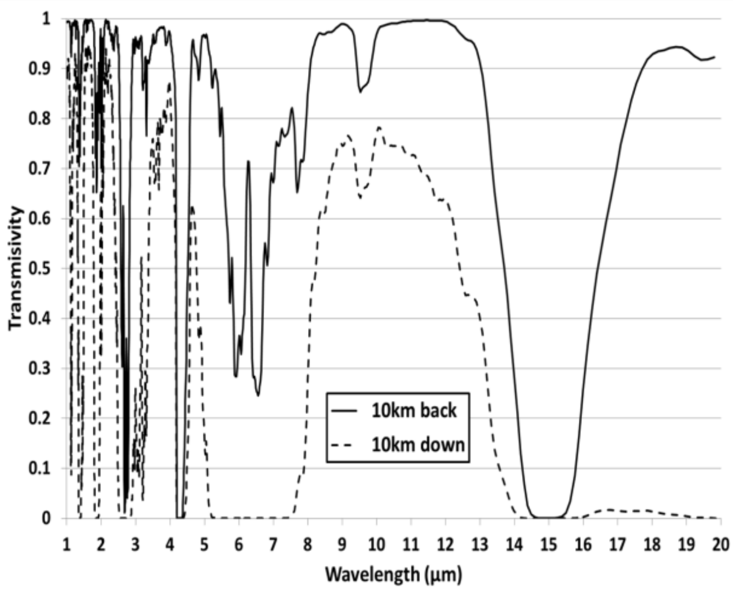

Fig. 15 Transmissivity for different observation positions in the case of the tropical atmosphere.

Based on the atmospheric transmissivity information, IR signatures were recalculated by considering atmospheric effects. As shown in Figs. 16 and 17, in all cases, IR signatures were reduced on average, and, in particular, IR signatures were significantly reduced in the wavelengths of 4.3-4.5μm (CO_2) and 5.5-7.5μm (H_2O). Further, red spikes that appear at wavelengths of 4.3μm or higher due to absorption by CO_2 were clearly observed. On the other hand, blue spikes that appear at wavelength of 4.3μm or lower were found to be almost negligible. The reason behind this disparity is that initial IR signatures used to take into account atmospheric effects have very small values at wavelengths of 4.3μm or lower. Also, while the red spikes remained unchanged for different seasons, as shown in Fig. 16, they had higher values as the observational distance became shorter, as shown in Fig. 17. This is because the distribution of CO_2 in the atmosphere remains essentially the same regardless of seasonal changes, and lower IR signatures are absorbed as the observation distance becomes shorter.

Moreover, IR signatures were drastically reduced when the detector was located lower, as shown in Fig. 18. In this situation, IR signatures had to pass through the high-density atmosphere as they headed toward the detector located at lower altitude, and therefore were absorbed more during the path. It was also found that, in the wavelengths of 5.5-7.5μm, IR signatures almost vanished, since most of those IR signatures were absorbed by the high concentration of H_2O in the atmosphere.

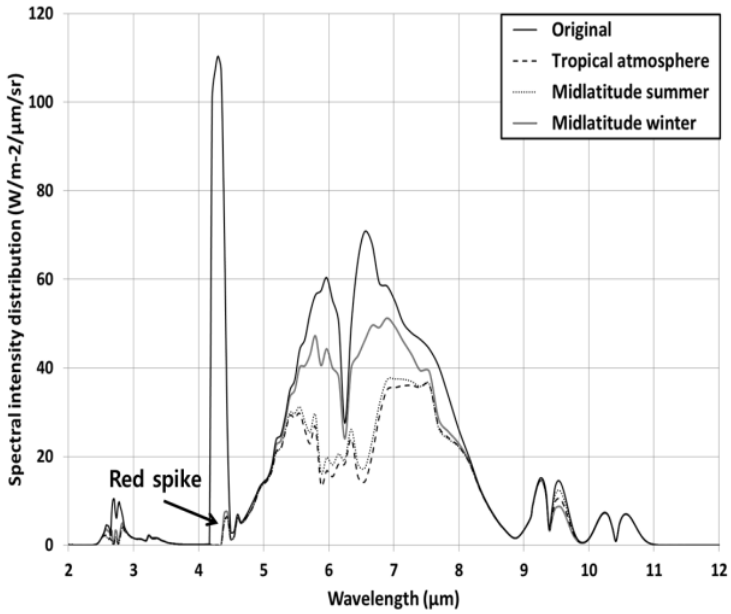

Fig. 16 IR signature for different seasons in the case of the observation distance 10km.

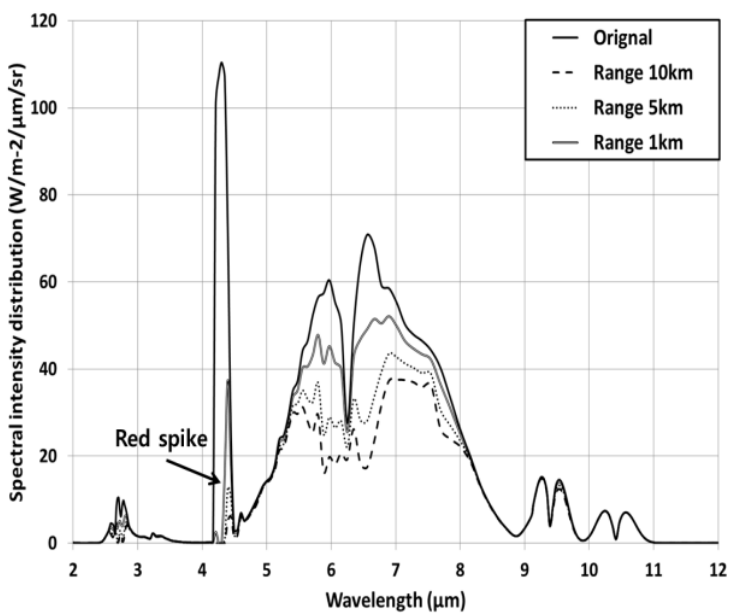

Fig. 17 IR signature for different distances in the case of the tropical atmosphere.

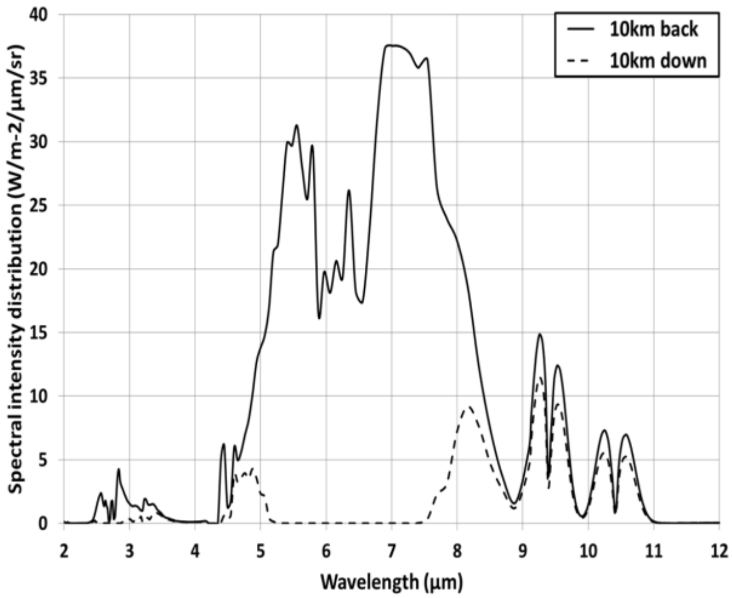

Fig. 18 IR signature for different observation positions in the case of the tropical atmosphere.

D. Effects of Different Nozzle Configurations on the Lock-on Range

An aircraft with jet engine has a high radiant intensity in order of 100-1000 W/sr, rendering very vulnerable to IR guided missiles. The lock-on range is the measure of aircraft susceptibility to IR guided missiles and can be determined primarily by the IR emissions of target aircraft and the detection capability of IR sensor [13,26]. When atmospheric transmissivity is taken into account, the lock-on range R_{LO} may be expressed as

$$R_{LO}^2 = \frac{I_c \eta_a}{(S/N)NEI}, \tag{5}$$

where I_c, η_a represent the contrast intensity of infrared emission from aircraft (W/sr) and the atmospheric transmission efficiency, respectively. And, $(S/N)\cdot NEI$ is the missile sensor's threshold for detection, (S/N) is the signal-to-noise ratio, and NEI is the noise equivalent irradiance.

The lock-on range can then be used to quantify the aircraft susceptibility and the effects of the IR reduction schemes developed for low-observable aircraft design on the aircraft susceptibility. In addition, when, for the sake of simplicity, the aircraft IR signal is assumed to emit isotropically in a plane with the same altitude, the lock-on envelope, a circle in the horizontal plane having radius R_{LO}, can be defined. In this study, in order to investigate the effects of deformed nozzles with high aspect ratio and large curvature on the lock-on range (equivalently, the lock-on envelope), equation (5) was solved for the case of the plume IR intensity in 3-5 μm band for different nozzle shapes. Since the atmospheric transmission efficiency in equation (5) varies depending on the distance between the aircraft and the seeker, equation (5) was calculated through the iterative method. In the calculation, the signal and noise ratio (*S/N*) and *NEI* were assumed 10.0 and 2.5×10^{-8} W/m^2/Sr, respectively, the typical IR sensor characteristics [27].

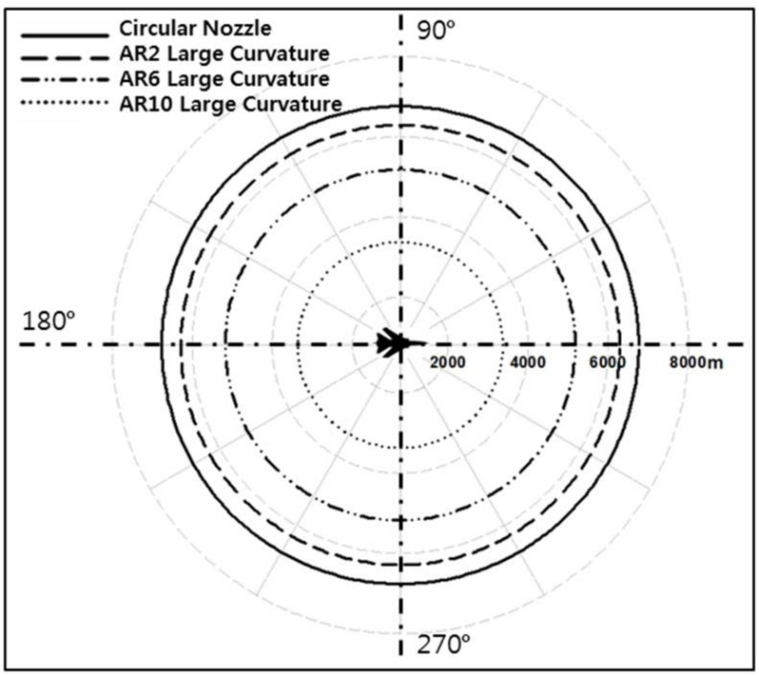

Fig. 19 Lock-on envelope of different nozzle shapes.

As expected, the lock-on range associated with the plume IR was found reduced considerably with increasing curvature and aspect ratio in nozzle shape, as shown in Fig. 19. In particular, while the reduction was small in the case of nozzle with a small aspect ratio (for example, 2.0), it was significant in the case of nozzle with high aspect ratio 10.0. In summary, it was shown that, in comparison with the original circular nozzle, the substantial reduction in the lock-on range (about 55%) is possible for deformed nozzles with the high aspect ratios.

VI. Conclusions

This study analyzed the effects of nozzle shapes and atmospheric conditions on plume IR signatures with the aim of developing a better nozzle design for aircraft IR reduction. Using an engine performance analysis program, a basic circular convergent nozzle was first selected. Various S-shaped nozzle configurations were then designed by varying the aspect ratio and the curvature of the circular convergent nozzle. A thermal flow field analysis was also conducted for the nozzles designed in this manner.

From the CFD results, compared to the circular nozzle, the average temperature at the outlet and wall of deformed non-circular nozzle shapes was found to decrease as much as 6%. Also, as the curvature and aspect ratio of the nozzle increased, the thrust was reduced up to 10.7%. This study also showed that plumes from the geometrically deformed nozzles were generally shorter and distributed more widely compared to those of the circular nozzle. Further, although both of aspect ratio and curvature contributed to the reduction of the average and maximum temperature in the plumes, the aspect ratio turned out to play a more critical role in the shortening and widening of high-temperature core plumes. For example, in the case of a high aspect ratio, high-temperature gases exhausted from the nozzle were distributed widely and were then more intensively mixed with the cold air of the external atmosphere. This led to considerable shortening of the length of core plumes, as much as half of that of the basic circular nozzle.

In the next step, the IR signatures of the nozzle were calculated based on thermal flow field data obtained through CFD analysis. The results showed that, while signature levels were reduced at the direct rear of the nozzle, higher IR signatures were observed on the left and rights sides of the nozzle due to a wider distribution of plumes, caused by increased aspect ratios. Also, as the plumes formed in a downward direction, higher IR signatures were observed in the downward direction.

Further, the atmospheric transmission according to change of seasons and observational distances was analyzed, and IR signatures were recalculated by taking into account atmospheric effects. It was found that IR signatures decreased significantly in the CO_2 band when the season was summer and the observational distance was shorter. That is, in summer, when the atmosphere contains more H_2O, IR signatures were more reduced relative to those in winter. Also, as the observational distance increased, IR signatures were found to be reduced substantially, since IR signatures from the nozzle had to pass through a longer atmospheric layer. In all cases, red spikes, which are caused by the absorption of signatures by CO_2 in the 4.3μm band, were observed, and in particular, as the observational distance became shorter, the maximum value of the red spikes increased due to reduced impacts of CO_2. In this manner, qualitative and quantitative data regarding plume IR signatures according to nozzle shapes and atmospheric conditions were obtained. Lastly, the lock-on range, the measure of aircraft susceptibility to IR guided missiles, was calculated for different nozzle configurations and was compared with the basic circular shape.

The present study was limited to the analysis of gaseous plume IR signatures due to their dominant role in aircraft IR study. However, we believe that continuous IR signatures associated with the hot solid surfaces of the nozzle will remain crucially important, in particular, in the longwave (8-16μm) band. Further, as the final outcome of IR analysis, the problem of calculating the lethal envelopes taking into account the missile capabilities like the relative velocity between aircraft and missile, and missile burn out time should be considered. Extension of the present study to these topics will be reported in due course.

Acknowledgments

This work has been supported by the Low Observable Technology Research Center Program of the Defense Acquisition Program Administration and Agency for Defense Development, Republic of Korea.

References

[1] Simmons, F. S., *Rocket Exhaust Plume Phenomenology*, The Aerospace Press, 2000.

[2] Hudson, R. D. Jr., *Infrared System Engineering*, Wiley, 1969.

[3] Ball, R. E., *The Fundamentals of Aircraft Combat Survivability Analysis and Design*, AIAA Education Series, 2nd Edition, 2003.

[4] Howe, D., “Introduction to Basic Technology of Stealth Aircraft: Part 1-Basic Considerations and Aircraft Self-Emitted Signals (Passive Considerations),” *Journal of Engineering for Gas Turbine and Power*, Vol. 113, No. 75, 1991, pp. 75-79.

[5] Rao, G. A., and Mahulikar, S. P., “Integrated Review of Stealth Technology and Its Role in Airpower,” *The Aeronautical Journal*, Vol. 106, No. 1066, 2002, pp. 629-641.

[6] MIL-E-5007D, *Military Specification: Engines, Aircraft, Turbojet and Turbofan, General Specification For*, The Department of Defense (US), 1973, pp. 56-57.

[7] Thompson, J., and Birk, A. M., “Design of an Infrared Signature Suppressor for the Bell 205(UH-1H) Helicopter Part 1: Aerothermal Design,” *11th CASI Propulsion Symposium*, 2010.

[8] Decher, R., “Infrared Emissions from Turbofans with High Aspect Ratio Nozzle,” *Journal of Propulsion and Power*, Vol. 20, No. 3, 2004, pp. 527-532.

[9] Mahulikar, S. P., Sonawane, H. R., and Rao, G. A., “Infrared Signature Studies of Aerospace Vehicles,” *Progress in Aerospace Sciences*, Vol. 43, Nos. 7-8, 2007, pp. 218-245.

[10] Mahulikar, S. P., Rao, G. A., and Kolhe, P. S., “Infrared Signatures of Low Flying Aircraft and Their Rear Fuselage Skin’s Emissivity Optimization,” *Journal of Aircraft*, Vol. 43, No. 1, 2006, pp. 226-232.

[11] Mahulikar, S. P., Rao, G. A., Sane, S. K., and Marathe, A. G., “Aircraft Plume Infrared Signature in Nonafterburning Mode,” *Journal of Thermophysics and Heat Transfer*, Vol. 19, No. 3, 2005, pp. 413-415.

[12] Rao, G. A., and Mahulikar, S. P., “Effect of Atmospheric Transmission and Radiance on Aircraft Infrared Signatures,” *Journal of Aircraft*, Vol. 42, No. 4, 2005, pp. 1046-1054.

[13] Rao, G. A., and Mahulikar, S. P., “New Criterion for Aircraft Susceptibility to Infrared Guided Missiles,” *Aerospace Science and Technology*, Vol. 9, 2005, pp. 701-712.

[14] Mahulikar, S. P., Kolhe, P. S., and Rao, G. A., “Skin Temperature Prediction of Aircraft Rear Fuselage with Multi-mode Thermal Model,” *Journal of Thermophysics and Heat Transfer*, Vol. 19, No. 1, 2005, pp. 114-124.

[15] Mahulikar, S. P., Sane, S. K., Gaitonde, U. N., and Marathe, A. G., “Numerical Studies of Infrared Signature Levels of Complete Aircraft,” *Aeronautical Journal*, Vol. 105, No. 1046, 2001, pp. 185-192.

[16] Rao, G. A., and Mahulikar, S. P., "Aircraft Powerplant and Plume Infrared Signature Modeling and Analysis," *43rd AIAA Aerospace Sciences Meeting and Exhibit*, Reno, Nevada, AIAA 2005-221, 2005.

[17] Mattingly, J. D., Heiser, W. H., and Pratt, D. T., *Aircraft Engine Design*, AIAA Education Series, 2nd Edition, 2002.

[18] *CFD-FASTRAN Software Version 2009*, ESI, Paris, France, 2015.

[19] Kneizys, F. X., Shettle, E. P., Abreu, L. W., Chetwynd, J. H., Amderson, G. P., Gallery, W. O., Selby, J. E. A., and Clough, S. A., *User Guide to LOWTRAN 7*, Air Force Geophysics Laboratory, AFGL-TR-88-0177, No. 1010, 1988.

[20] Kang, D. W., Kim, J. Y., Myong, R. S., and Kim, W. C., "Computational Investigation of the Effect of UAV Engine Nozzle Configuration on Infrared Signature," *Journal of The Korean Society for Aeronautical & Space Sciences*, Vol. 41, No. 10, 2013, pp. 779-787 (in Korean).

[21] Wilcox, D. C., *Turbulence Modeling for CFD*, 3^{rd} Edition, DCW Industries, 2006.

[22] Oberkampf, W. L., and Roy, C. J., *Verification and Validation in Scientific Computing*, Cambridge University Press, 2010.

[23] Thornock, R. L., and Brown, E. F., "An Experiment Study of Compressible Flow Thorough Convergent-Conical Nozzles, Including a Comparison with Theoretical Results," *Journal of Basic Engineering*, Vol. 94, 1972, pp. 926-930.

[24] AIAA Propulsion Aerodynamics Workshop, http://www.aiaa-propulsionenergy.org/PAW02/, (12/2015).

[25] Grosshandler, W. L., "RADCAL: A Narrow-Band Model for Radiation Calculations in a Combustion Environment," *National Technical Information Service*, TN 1402, 1993.

[26] Kim, M. J, Kang, D. W., Myong, R. S., and Kim, W. C., "Investigation of the Effects of UAV Nozzle Configurations on Aircraft Lock-on Range," *Journal of The Korean Society for Aeronautical & Space Sciences*, Vol. 43, No. 3, 2015, pp. 204-212 (in Korean).

[27] Hytönen, H., *Utilization of Air-to-Air Missile Seeker Constrains in the Missile Evasion*, Project Report, Helsinki University of Technology, 2004.